NASA/TM–2020-220579

A 3D model to predict explicit morphologies and volume fraction of lack-of-fusion pores generated in selective laser melting processes

Saikumar R. Yeratapally
National Institute of Aerospace, Hampton, Virginia

Albert Cerrone
University of Notre Dame, Notre Dame, Indiana

Ming Tang
Carnegie Mellon University, Pittsburgh, Pennsylvania

Edward H. Glaessgen
NASA Langley Research Center, Hampton, Virginia

March 2020

NASA STI Program . . . in Profile

Since its founding, NASA has been dedicated to the advancement of aeronautics and space science. The NASA scientific and technical information (STI) program plays a key part in helping NASA maintain this important role.

The NASA STI program operates under the auspices of the Agency Chief Information Officer. It collects, organizes, provides for archiving, and disseminates NASA's STI. The NASA STI program provides access to the NTRS Registered and its public interface, the NASA Technical Reports Server, thus providing one of the largest collections of aeronautical and space science STI in the world. Results are published in both non-NASA channels and by NASA in the NASA STI Report Series, which includes the following report types:

- TECHNICAL PUBLICATION. Reports of completed research or a major significant phase of research that present the results of NASA Programs and include extensive data or theoretical analysis. Includes compilations of significant scientific and technical data and information deemed to be of continuing reference value. NASA counter-part of peer-reviewed formal professional papers but has less stringent limitations on manuscript length and extent of graphic presentations.

- TECHNICAL MEMORANDUM. Scientific and technical findings that are preliminary or of specialized interest, e.g., quick release reports, working papers, and bibliographies that contain minimal annotation. Does not contain extensive analysis.

- CONTRACTOR REPORT. Scientific and technical findings by NASA-sponsored contractors and grantees.

- CONFERENCE PUBLICATION. Collected papers from scientific and technical conferences, symposia, seminars, or other meetings sponsored or co-sponsored by NASA.

- SPECIAL PUBLICATION. Scientific, technical, or historical information from NASA programs, projects, and missions, often concerned with subjects having substantial public interest.

- TECHNICAL TRANSLATION. English-language translations of foreign scientific and technical material pertinent to NASA's mission.

Specialized services also include organizing and publishing research results, distributing specialized research announcements and feeds, providing information desk and personal search support, and enabling data exchange services.

For more information about the NASA STI program, see the following:

- Access the NASA STI program home page at http://www.sti.nasa.gov

- E-mail your question to help@sti.nasa.gov

- Phone the NASA STI Information Desk at 757-864-9658

- Write to:
  NASA STI Information Desk
  Mail Stop 148
  NASA Langley Research Center
  Hampton, VA 23681-2199

NASA/TM–2020-220579

A 3D model to predict explicit morphologies and volume fraction of lack-of-fusion pores generated in selective laser melting processes

Saikumar R. Yeratapally
National Institute of Aerospace, Hampton, Virginia

Albert Cerrone
University of Notre Dame, Notre Dame, Indiana

Ming Tang
Carnegie Mellon University, Pittsburgh, Pennsylvania

Edward H. Glaessgen
NASA Langley Research Center, Hampton, Virginia

National Aeronautics and
Space Administration

Langley Research Center
Hampton, Virginia 23681-2199

March 2020

Acknowledgements

The development of this work was initiated through funding from the NASA Aeronautics Research Mission Directorate's Transformative Tools and Technologies project.

Available from:

NASA STI Program / Mail Stop 148
NASA Langley Research Center
Hampton, VA 23681-2199
Fax: 757-864-6500

Abstract

The performance of an additively manufactured (AM) component is dependent on the distribution of process-induced defects in addition to the complex microstructure of the material, surface roughness of the component and the process-induced residual stresses. For instance, it has been well demonstrated that lack-of-fusion (LoF) pores produced in the selective laser melting (SLM) AM process can significantly limit the fatigue performance of the material. Although two-dimensional (2D) models exist to predict the 2D profiles of LoF pores, the 2D pore profiles cannot be directly inserted into a three-dimensional (3D) microstructure domain that is output from several prevailing process simulation packages. A few commercial packages that simulate the SLM process can predict LoF pores in a 3D domain, but the morphologies of LoF pores are voxelated and hence do not capture sharp corners of the pores, thereby obviating their use in fatigue crack initiation studies.

In order to address the aforementioned gaps, a high-fidelity model that predicts not only the volume fraction, but also the explicit 3D morphologies and spatial distributions of LoF pores has been developed using a computer aided design-based environment. The model has been partially validated for Ti-6Al-4V alloy by comparing the predictions of the volume fraction of LoF pores predicted by the model with experimental data obtained from the literature. Absolute error in predicted volume fraction of LoF pores varied between 5.16% and 1.87% for energy density values between 13 J/mm^3 and 45 J/mm^3 where a significant amount (over 3% volume fraction) of LoF porosity was measured. The absolute error was within 1.87% for energy density values greater than 45 J/mm^3.

1. Introduction

The selective laser melting (SLM) process produces multiple types of process-induced pores including: i) lack-of-fusion (LoF) pores [1-4], ii) keyhole pores [2,3], iii) entrapped gas pores [3], and iv) oxide-driven pores [5]. In addition to porosity, surface roughness and balling are the other types of defects, which, if present, can lead to the sub-optimal performance of SLM-built materials. The complex interplay between defects and microstructure control the mechanical behavior of parts produced through the SLM process.

Distinct process-specific mechanisms lead to the formation of the different types of defects in the SLM process. LoF pores are formed when a low power, high velocity laser is used that is unable to fully melt the powder particles. Using large hatch spacing also leads to the formation of LoF pores [4]. Additionally, spatter can increase the probability of the formation of LoF pores [6]. Keyhole pores are formed when a high energy laser moving with a low velocity creates deep melt pools that become unstable and lead to formation of bubbles that are unable to escape as they are trapped by the advancing solidification front [7]. Entrapped gas pores are the pores within the powder particles that get trapped in the part [3]. Oxides are formed from native oxide film on powder particles and from the oxidation of metal vapor during part manufacturing [8]. Oxide-driven porosity is caused by a thin oxide film surrounding the melt pool which inhibits fusion and sticking (i.e. wetting) to the surrounding solid [8,9].

The morphological attributes of defects and their spatial distribution within the bulk of the material influence its mechanical behavior [10-18]. Based on high resolution X-Ray computed tomography (CT) studies [2,3,19], it is evident that LoF pores have highly irregular geometry and are characterized by high aspect ratios and sharp corners that act as drivers for strain localizations that may initiate fatigue cracks [3,4,20]. Large LoF pores generate high stress-intensity factors and degrade the ductility of SLM-built components, while small LoF pores promote fatigue crack initiation [20]. Oxide-driven pores are also characterized by complex shapes of pores located in the vicinity of oxide particles [5,8]. On the other hand, keyhole and entrapped gas pores have smooth morphologies and are nearly spherical in nature, and consequently accumulate less strain in comparison to irregular LoF pores of similar size [21].

Recently, computational studies have been undertaken to study the effect of size, shape, and spatial distribution of pores on mechanical performance attributes of metallic materials. Using crystal plasticity finite element (CPFE) simulations, Prithivirajan et al. [22] showed that there exists a critical pore size beyond which fatigue crack initiation occurs near the vicinity of pores rather than at crystallographic features. Cunningham et al. [23], using a CPFE framework, showed that large pores accumulate higher strains compared to small pores. By embedding idealized (spherical) keyhole pores and idealized (super-ellipsoidal) LoF pores into the same microstructural volume, Yeratapally et al.[21] conducted CPFE analysis to quantitatively show that the LoF pores accumulate significantly more strain compared to an idealized keyhole pore of the same size. Kabir et al. [24], using a finite element framework, compared pores with convex and concave boundaries to investigate the von Mises stress profile in the vicinity of the pores. Pores with convex boundaries simulate the presence of keyhole or entrapped gas pores, whereas the pores with concave boundaries simulate the effect of LoF pores. It was shown that the pores with concave boundaries have highly inhomogeneous stress distribution with multiple, narrow plastic zones, unlike the stress profile surrounding pores with convex boundaries. Using an analytical model representing an isolated pore in a homogeneous elastic medium, Sobotka et al. [25] showed that maintaining a spherical pore geometry and reducing the pore size are desirable to promote higher fatigue lives.

Based on computational studies supported by experimental observations, it is evident that LoF pores with irregular morphologies play a role in considerably degrading the mechanical properties of SLM-built materials. This underscores the importance of the process parameters to eliminate the formation of LoF pores. Minimizing porosity by producing several specimens, each with a different combination of process parameters and characterizing porosities in each of the specimens using non-destructive evaluation techniques is a costly and time-consuming process. In order to overcome this barrier, a high-fidelity computational model that links process parameters to the explicit three-dimensional (3D) morphologies and distribution of LoF pores, which is the focus of the current study, is important. While oxide-driven pores have irregular morphologies, as well, simulating their formation is beyond the scope of the current study.

Over the past few years, considerable research has been dedicated to developing predictive models that link process parameters to the formation of LoF pores. Tang et al. [26,27] developed a two-dimensional (2D) model to predict the size, shape and distribution of LoF pores in a 2D simulation domain. Mukherjee et al. [28] used a heat transfer and fluid flow model to build a 2D model that solves for the 2D morphologies and area fraction of LoF pores. Further, he formulated a dimensionless number to help process engineers mitigate the formation of LoF pores. Two-dimensional descriptions, however, are somewhat limited given that the SLM process is inherently multi-dimensional. For example, 2D pore profiles from these 2D process models cannot be directly inserted into a 3D microstructure domain output from the prevailing process simulation packages. Incorporating these profiles would facilitate the study of the interplay between the complex heterogeneities of the microstructure and the LoF pores. Hence, prediction of explicit morphologies and spatial distribution of LoF pores in 3D is important to fully characterize the scatter in mechanical properties. Although there are commercial packages [29,30] that predict LoF pores in a 3D domain, their morphologies are voxelated and hence do not capture sharp corners of the pores, thereby obviating their use in fatigue crack initiation studies. The current work is aimed at addressing the aforementioned gaps that exist in modeling LoF pores. The LoF porosity model proposed in the current study is built on the foundation of the 2D model developed by Tang et al. [26,27] and extends it to 3D to extract explicit 3D computer aided design (CAD) geometries of LoF pores by taking the process parameters and thermal properties of materials as input.

A detailed overview of the 3D LoF porosity framework is provided in Section 2. Thereafter, a partial validation of the framework is given in Section 3. Conclusions of the study are presented in Section 4.

2. 3D lack-of-fusion model

The 3D LoF model discussed in this work is built using the framework of the 2D model developed by Tang et al. [8,26,27] as the baseline. CAD tools available in ABAQUS [31] are leveraged to build the 3D LoF model. Generation of 3D LoF pore geometries is accomplished in five steps: i) obtain the melt pool width from the Rosenthal equation, which takes into account both the process parameters and relevant material properties, ii) construction of a bi-elliptical melt pool cross-section, as discussed in Tang et al. [26,27], and extruding it into a single scan track, iii) produce multiple single tracks side-by-side (on the XY plane, as shown in Fig. 1) in such a way that each scan track is separated from the neighboring scan track by the hatch spacing, H, thereby achieving a single scan layer, iv) three dimensional arrangement of multiple scan layers in such a way that consecutive scan layers are separated vertically (in Z direction, as depicted in the schematic shown in Fig. 1) by the layer thickness, L, and is rotated from the preceding layer by the hatch rotation, θ, and v) isolating non-overlapping regions, converting them into 3D CAD geometries. A schematic of the 3D CAD model with melt pool layers is shown in Fig. 1. It must be noted that there is no hatch rotation used for the example shown in Fig. 1. Each of the five steps are discussed in detail in the following sub-sections.

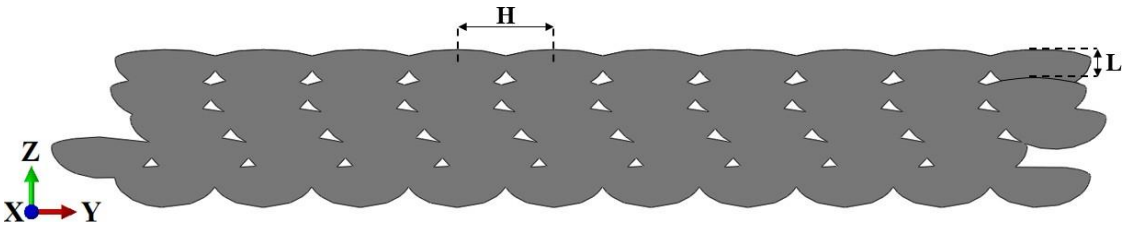

Fig. 1 ZY plane showing 5 melt pool layers. The definitions of H and L are shown.

2.1 Obtaining melt pool width using Rosenthal equation

For the purpose of the current study, the cross-section of a melt pool scan track is assumed to be bi-elliptical, as shown in Fig. 2, based on the work of Tang et al. [26,27]. The width, depth, and bead height of the melt pool are represented by W, D and R, respectively. Given the power (Q) and velocity (V) of the laser, the melt pool width, W, is obtained by analytically solving the Rosenthal equation for a special case where D is assumed to be half of W. For this special case (D=W/2), the relation between Q, V, W, and other material-specific parameters like the melting temperature (T_f), absorptivity (α), thermal conductivity (k), ambient temperature (T_o), density (ρ), and heat capacity (C) is given by Eq. 1, adapted from the work of Tang [8]. W was obtained by solving Eq. 1.

$$\alpha Q = \pi k(T_f - T_o)W + 0.125e\pi\rho C(T_f - T_o)VW^2 \quad (1)$$

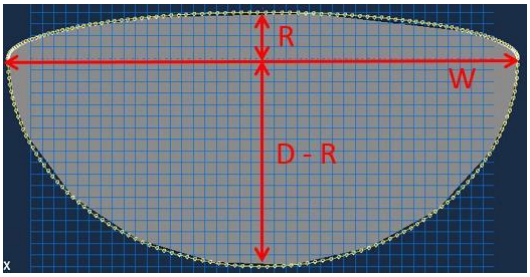

Fig. 2. Schematic of an idealized bi-elliptical cross-section of a melt pool scan track.

For the purpose of the current study, Ti-6Al-4V alloy has been chosen. Although the Rosenthal equation has been rigorously validated for the conduction mode, a customary validation effort is undertaken in the current work to verify that the melt pool widths obtained from Eq. 1 are comparable to experimental values. Experimental melt pool widths for various process parameter combinations are obtained from the values furnished in the literature for Ti-6Al-4V alloy [32]. Figure 3 shows the comparison between the model predictions and experimental data as a function of laser power for various velocities. From this data, it is evident that the model is predicting the melt pool widths reasonably well. Table 1 shows the values of the material properties used in Eq. 1 to solve for the melt pool widths. The value for absorptivity (α) was chosen based on the work of Yang et al. [33], while the values for the rest of the parameters were borrowed from the work of Tang et al. [5,8]. It must be noted that there would be a certain level of uncertainty in the values of parameters, α, k, C and ρ at temperature T_f. Since the purpose of the current work is to demonstrate the framework of the 3D LoF model, the uncertainties in the aforementioned parameters will be ignored.

Table 1. Ti-6Al-4V alloy material properties used in Rosenthal equation

Parameter (units)	Value
α	0.38
T_f (K)	1913
T_o (K)	303
$k\left(\frac{W}{m\,K}\right)$	6.7
$C\left(\frac{J}{kg\,K}\right)$	526
$\rho\left(\frac{kg}{m^3}\right)$	4430

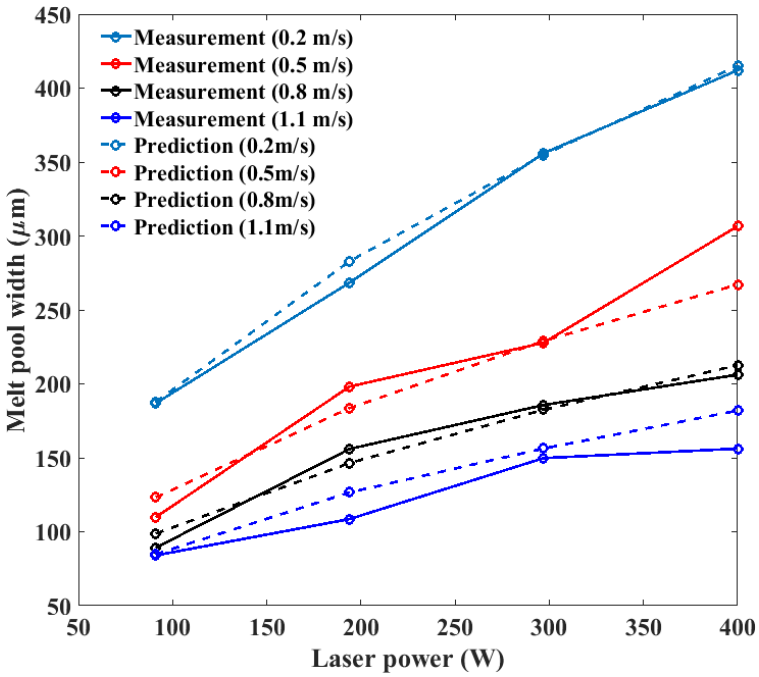

Fig. 3. Comparison of experimental measurements of melt pool width (for varying laser power and scan velocity) of SLM built Ti-6Al-4V material with predictions from the Rosenthal equation.

2.2 Constructing an idealized scan track with bi-elliptical melt pool cross-section

It is assumed that the cross-section of the melt pool remains constant throughout the scan path. Hence, the scan track was modeled by simply extruding the bi-elliptical melt pool cross section. The length of the scan track is arbitrarily chosen by the user. In choosing the length of the scan track for this study, measures were taken to ensure that it was not too small to render no LoF pores and not too large to overburden ABAQUS' CAD package. For the build in Fig. 4, W, D and R were taken to be 99.4 μm, 49.7 μm, and 10 μm, respectively. A scan track modeled using the aforementioned parameters is shown in Fig. 4(a). A 3D scan track with varying cross-section can be readily generated in a CAD framework, for example, using the LOFT functionality in AUTOCAD [32], but modeling a scan track with varying cross section is beyond the scope of the current work.

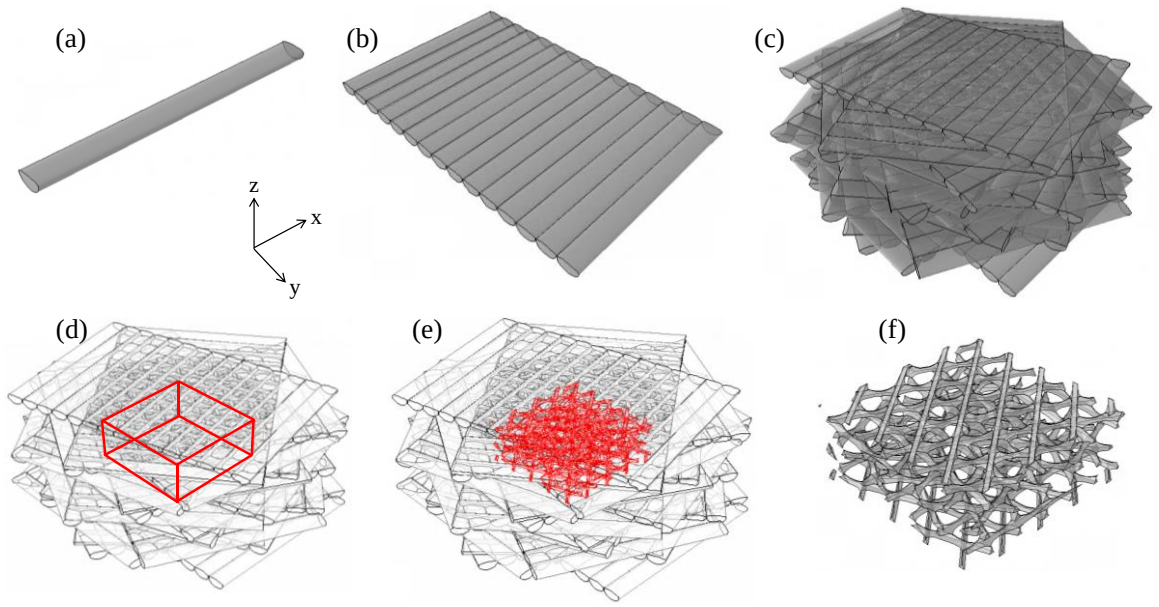

Fig. 4. (a) An idealized scan track with a constant bi-elliptical cross section. (b) A scan layer built by laying the scan tracks side-by-side. (c) Multiple scan layers arranged on top of each other, separated by a specified layer thickness, in such a way that each consecutive layer is rotated by a specified hatch rotation. (d) Box used for LoF pore extraction. The scan tracks cut this box, and the resulting fragments within the box are the desired LoF pore morphologies. (e) LoF pore morphologies highlighted among scan tracks. (f) Explicit morphologies of LoF pores.

2.3 Constructing scan layers

An idealized scan layer is modeled by placing a scan track alongside another (as shown in Fig. 4(b)) in such a way that any two consecutive scan tracks are offset by H. In order to achieve this, multiple instances of the idealized scan track are created in the assembly module in ABAQUS. Based on the work of Dilip et al. [35], H was chosen to be 100 µm. Non-overlapping melt pools (W<H) result in an enormous amount of LoF porosity and should always be avoided. For the purpose of demonstrating the framework, the value of W was kept 99.4 µm (as discussed in Section 2.2) to achieve non-overlapping melt pools that would result in clearly distinguishable morphologies of LoF pores. Based on the aforementioned values of W, D, R and H, the CAD drawing shown in Fig. 4(b) depicts a single scan layer that constitutes consecutive scan tracks that do not overlap with one another. Further, in order to replicate a simple build, multiple scan layers, like the one shown in Fig. 4(b), are stacked on top of each other. Figure 4(c) shows twenty such scan layers. In the build shown in Fig 4(c), L and θ are taken to be 30 µm and 67°, respectively, based on the work of Tang et al. [5,8].

2.4 Extracting LoF pores

Extracting LoF pores is the most computationally expensive step of the entire process. First, a solid box is fit inside multiple scan layers such that it is fully enveloped by the tracks, Fig 4(d). Next, using a subtract boolean operation in ABAQUS, the scan

layers are used to cut the solid box. The uncut regions of the box, effectively regions where no scan track traversed, are the desired LoF pore geometries. The regions shown in red in Fig. 4(e) are the LoF pore regions. The explicit morphologies of the LoF pores formed in the build are shown in Fig. 4(f).

It is noteworthy that Steps 1-5 are automated in a Python-based macro which can be executed within ABAQUS CAE. The macro accepts eight inputs: (1) desired number of scan tracks in the x-y plane, (2) scan length, (3) number of layers, (4) hatch rotation - θ, (5) hatch spacing - H, (6) layer thickness - L, (7) melt pool width - W (from Rosenthal equation), and (8) melt pool depth - D. When considering approximately 300 scan tracks, the macro runs in a couple of minutes on a desktop workstation with a 3rd generation Intel Core i7 processor and 24 GB of RAM.

3. Validation of the model

The predictions made by the 3D LoF porosity model have been validated against experimental data published in the literature. Specifically, the volume fraction of LoF porosity, υ, measured for various combinations of process parameters has been used as a validation metric in the current study. The variation of υ with respect to the energy density, E (defined as $\frac{P}{VHL}$), has been obtained from the work of Dilip et al. [35] for Ti-6Al-4V alloy, and this data will be compared to the predictions from the model for the purpose of validation. It must be noted that this is considered only a partial validation since only volume fraction of LoF pores are being compared to experimental measurements, and not the explicit morphologies and spatial distributions of the pores. The parameters of H, L and θ have been assigned fixed values 100 µm, 30 µm and 67°, respectively, throughout the validation study. Table 2 shows various combinations of process parameters that have been chosen to study the variation of υ with respect to E.

Table 2. Process parameters used in the validation study. Values have been chosen based on the experimental studies of Dilip et al. [35]

P (W)	V $\left(\frac{mm}{s}\right)$	E = $\frac{P}{VHL}\left(\frac{J}{mm^3}\right)$
50	500	33.33
50	750	22.22
50	1000	16.67
50	1200	13.89
100	750	44.44
100	1200	27.78
150	500	100
150	750	66.00
150	1000	50.00

Figure 5 compares the predictions of the 3D LoF model with experimental data. Absolute error in the prediction of volume fraction of LoF porosity is shown in Fig. 6. The absolute

error is between 5.16% and 1.87% for energy density values between 13 J/mm^3 and 45 J/mm^3 where a significant amount (over 3% volume fraction) of LoF porosity was measured. The absolute error is within 1.87% for energy density values greater than 45 J/mm^3. Beyond the energy density value of 66 J/mm^3 the formation of keyhole pores is favored, and hence the LoF porosity prediction model is not applicable in this domain.

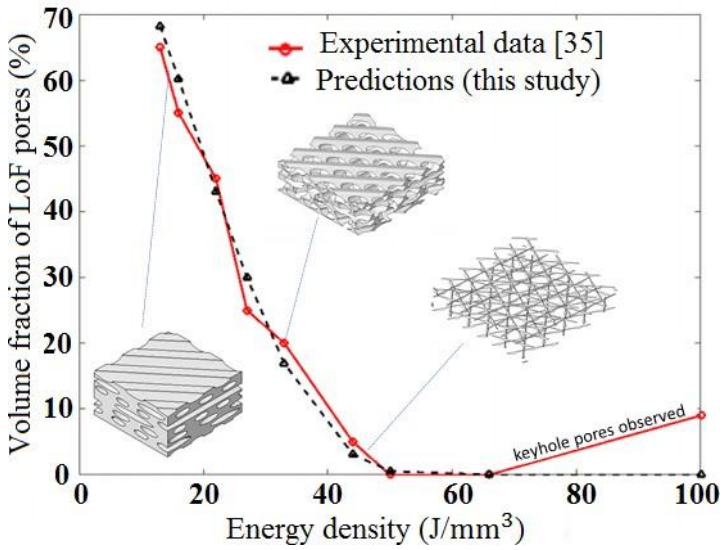

Fig. 5. Variation of LoF porosity with laser energy density (E) for Ti-6Al-4V alloy, as predicted by the 3D LoF model and that obtained from experiments [35]. Pore morphologies are shown for select energy densities.

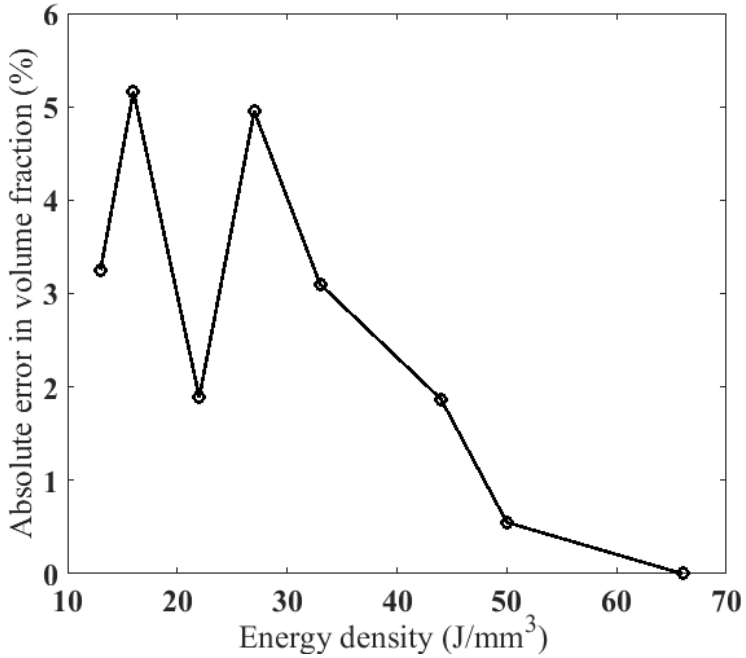

Fig. 6. Absolute error in predicted volume fraction of LoF pores for various energy densities.

4. Conclusions

This report details the extension of a pre-existing two-dimensional (2D) lack of fusion (LoF) porosity model [26,27] to three dimensions and the resulting CAD-based implementation. LoF porosity is caused by non-overlapping melt pools, a phenomenon dictated by melt pool geometries and scan path strategies. The model presented herein incorporates these two factors to create an assembly of three-dimensional (3D) scan tracks and subsequently generates geometries of non-overlapping (viz. not-melted) regions. This report includes partial validation of the model— its ability to predict pore volume fractions is demonstrated, but the resulting morphologies (which are crack-like and qualitatively mimic LoF pores) have yet to be experimentally validated.

The model was designed to be incorporated into multiscale simulation workflows wherein process-induced defects (such as the LoF species) are considered explicitly in life estimation. For example, the 3D LoF pore morphologies produced by this model could be incorporated directly into a process-informed 3D microstructural model (such as from SPPARKS [36]) for crystal-plasticity finite-element analysis with a high-performance FE driver like ScIFEN. Given the CAD-based model's relatively short run times (on the order of a couple of minutes), uncertainty quantification is possible. For example, stochastic reduced order models [37,38] could be used to propagate uncertainty through this crystal plasticity finite element framework to assess the influence of a particular process parameter (e.g. laser power) on lifing capability.

References

[1] Tang, M., Pistorius, P. C., "Anisotropic Mechanical Behavior of AlSi10Mg Parts Produced by Selective Laser Melting," *Journal of Materials,* Vol. 69, No. 3, 2017, pp. 516-522.

[2] Cunningham, R., Narra, S. P., Montgomery, C., Beuth, J., Rollett, A.D., "Synchrotron-Based X-ray Microtomography Characterization of the Effect of Processing Variables on Porosity Formation in Laser Power-Bed Additive Manufacturing of Ti-6Al-4V," *Journal of Materials,* Vol. 69, No. 3, 2017, pp. 479-484.

[3] Cunningham, R., Narra, S. P., Ozturk, T., Beuth, J., Rollett, A.D., "Evaluating the Effect of Processing Parameters on Porosity in Electron Beam Melted Ti-6Al-4V via Synchrotron X-ray Microtomography," *Journal of Materials,* Vol. 68, No. 3, 2016, pp-765-771.

[4] Brown, A., Zachary, J., Tilson, W., "Classification, Effects, and Prevention of Build Defects in Powder-bed Fusion Printed Inconel 718," *NASA Report Number M17-5848*, 2017.

[5] Tang, M., Pistorius, P. C., "Oxides, Porosity and Fatigue Performance of AlSi10Mg Parts Produced by Selective Laser Melting," *International Journal of Fatigue,* Vol. 94, No. 2, 2017, pp. 192-201.

[6] Guo, Q., Zhao, C., Escano, L.I., Young, Z., Xiong, L., Fezzaa, K., Everhart, W., Brown, B., Sun, T., Chen, L., "Transient dynamics of powder spattering in laser powder bed fusion

additive manufacturing process revealed by in-situ high-speed high-energy x-ray imaging," *Acta Materialia,* Vol. 151, 2018, pp. 169-180.
[7] Zhao, C., Fezzaa, K., Cunningham, R.W., Wen, H., Carlo, F.D., Chen, L., Rollett, A.D., Sun, T., "Real-time monitoring of laser powder bed fusion process using high-speed X-ray imaging and diffraction," *Scientific Reports,* 7:3602, pp. 1-11.
[8] Tang, M., "Inclusions, Porosity, and Fatigue of AlSi10Mg Parts Produced by Selective Laser Melting," *Ph.D. Thesis*, Carnegie Mellon University, Pittsburgh, PA, 2017.
[9] Louvis, E., Fox, P., Sutcliffe, C.J., "Selective laser melting of aluminium components," *J. Mater. Process. Technol.*, Vol. 211, No. 2, 2011, pp. 275–284.
[10] Tang, M., Pistorius, P.C., "Anisotropic Mechanical Behavior of AlSi10Mg Parts Produced by Selective Laser Melting," *Journal of Materials*, Vol. 69, No. 3, 2017, pp. 516-522.
[11] Romano, S., Brückner-Foit, A., Brandão, A., Gumpinger, J., Ghidini, T., Beretta, S., "Fatigue Properties of AlSi10Mg Obtained by Additive Manufacturing: Defect-based Modelling and Prediction of Fatigue Strength," *Engineering Fracture Mechanics,* Vol. 187, 2018, pp. 165-189.
[12] Romano, S., Patriarca, L., Foletti, S., Beretta, S., "LCF Behaviour and a Comprehensive Life Prediction Model for AlSi10Mg Obtained by SLM," *International Journal of fatigue,* Vol. 117, 2018, pp. 47-62.
[13] Romano, S., Beretta, S., Brandão, A., Gumpinger, J., Ghidini, T., "HCF Resistance of AlSi10Mg Produced by SLM in Relation to the Presence of Defects," *Procedia Structural Integrity,* Vol. 7, 2017, pp. 101-108.
[14] Williams, S.T., Withers, P.J., Prangnell, P.B., "*The Influence of Porosity on Fatigue Crack Initiation in Additively Manufactured Titanium Components*," *Scientific Reports,* Vol. 7:7308, 2017, pp.1-13.
[15] Almatani, R.A., "*The Effect of Pore Density and Distribution on Fatigue Weak Links in an A713 Cast Aluminum Alloy*," Master's Thesis, College of Engineering, Univ. of Kentucky, Lexington, KY, 2017.
[16] Tang, M., Pistorius, P.C., "Fatigue Life Prediction for AlSi10Mg Components Produced by Selective Laser Melting," *International Journal of Fatigue,* Vol. 125, 2019, pp. 479-490.
[17] Le, V.D., Saintier, N., Morel, F., Bellett, D., Osmond, P., "Investigation of the effect of porosity on the high cycle fatigue behaviour of cast Al-Si alloy by X-ray micro-tomography," *Int. J. Fatigue*, Vol. 106, 2018, pp. 24-37.
[18] Biswal, R., Zhang, X., Shamir, M., Mamun, A.A., Awd, M., Walther, F., Syed, A.K., "Interrupted fatigue testing with periodic tomography to monitor porosity defects in wire + arc additive manufactured Ti-6Al-4V," *Additive Manufacturing,* Vol. 28, 2019, pp.517-527.
[19] Kasperovich, G., Haubrich, J., Gussone, J., Requena, G., "Correlation between porosity and processing parameters in TiAl6V4 produced by selective laser melting," *Materials and Design,* Vol. 105, 2016, pp. 160-170.
[20] Zhang, B., Ham, K., Shao, S., Shamsaei, N., Thompson, S.M., "Effect of Heat Treatment and Hot Isostatic Pressing on the Morphology and Size of Pores in Additive Manufactured Ti-6Al-4V Parts," *Proceedings of the 28th Annual International Solid Freeform Fabrication Symposium*, 2017, pp. 107-114.

[21] Yeratapally, S.R., Lang, C.G., Glaessgen, E.H., "A Computational Study to Investigate the Effect of Defect Geometries on the Fatigue Crack Driving Forces in Powder-Bed AM Materials*," proceedings of AIAA SciTech 2020*, Orlando, FL.
[22] Prithivirajan, V., Sangid, M.D., "The Role of Defects and Critical Pore Size Analysis in the Fatigue Response of Additively Manufactured IN718 via Crystal Plasticity," *Materials & Design,* Vol. 150, No. 1, 2018, pp. 139-153.
[23] Cunningham, R., Nicolas, A., Madsen, J., Fodran, E., Anagnostou, E., Sangid, M.D., Rollett, A.D., "Analyzing the Effects of Powder and Post-processing on Porosity and Properties of Electron Beam Melted Ti-6Al-4V," *Materials Research Letters,* Vol. 5, No. 7, 2017, pp. 516-525.
[24] Kabir, M.R., Richter, H., "Modeling of Processing-Induced Pore Morphology in an Additively-Manufactured Ti-6Al-4V Alloy," *Materials,* Vol. 10, 2017, 1-15.
[25] Sobotka, J.C., Enright, M.P., McClung, R.C., "Application of Critical Distances to Fatigue at Pores," *Fatigue & Fracture of Engineering Materials & Structures,* 2019. doi:10.1111/ffe.13004.
[26] Tang, M., Pistorius, P.C., Beuth, J.L., "Prediction of Lack-of-Fusion Porosity for Powder Bed Fusion," *Additive Manufacturing,* Vol. 14, 2017, pp. 39-48.
[27] Tang, M., Pistorius, P.C., Beuth, J., "Geometric Model to Predict Porosity of Part Produced in Powder Bed System," *Proceedings of the Materials Science and Technology (MS&T) Conference*, Columbus, Ohio, 2015, pp. 129-135.
[28] Mukherjee, T., Debroy, T., "Mitigation of lack of fusion defects in powder bed fusion additive manufacturing," *Journal of Manufacturing Processes,* Vol. 36, 2018, pp. 442-449.
[29] Zhang, Q., Xie, J., Gao, Z., London, T., Griffiths, D., Oancea, V., "A metallurgical phase transformation framework applied to SLM additive manufacturing processes," *Materials and Design,* Vol. 166, 2019, 107618.
[30] "Tutorial 16: To Analyze Lack of Fusion and Hot Spots," *NetFabb (AutoDesk), URL*:https://knowledge.autodesk.com/support/netfabb/learn-explore/caas/CloudHelp/cloudhelp/2018/ENU/NETF-Utility-Simulation/files/GUID-D3D423E3-BB0E-474B-AB8C-A871BC443E1D-htm.html
[Retrieved 22nd March, 2020].
[31] ABAQUS FEA, URL: https://www.3ds.com/products-services/simulia/products/abaqus/ [URL retrieved 22nd March, 2020].
[32] Kusuma, C., "The Effect of Laser Power and Scan Speed on Melt Pool Characteristics of Pure Titanium and Ti-6Al-4V alloy for Selective Laser Melting," *Masters Thesis*, Wright State Univ., Dayton, OH, 2016.
[33] Yang, J., Sun, S., Brandt, M., Yan, W., "Experimental investigation and 3D finite element prediction of the heat affected zone during laser assisted machining of Ti6Al4V alloy," *Journal of Mat. Process. Tech*., Vol. 210, 2010, pp. 2215-2222.
[34] AutoCAD from AutoDesk, URL: https://www.autodesk.com [retrieved 22nd March, 2020].
[35] Dilip, J.J.S., Zhang, S., Teng, C., Zend, K., Robinson, C., Pal, D., Stucker, B., "Influence of processing parameters on the evolution of melt pool, porosity, and microstructures in Ti-6Al-4V alloy parts fabricated by selective laser melting," *Prog. Addit., Manuf.,* Vol. 2, 2017, pp. 157-167.
[36] SPPARKS Kinetic Monte Carlo Simulator, URL: https://spparks.sandia.gov/ [retrieved 22nd March, 2020].

[37] SROMPy, URL: https://github.com/nasa/SROMPy [URL retrieved 22nd March, 2020].
[38] Warner, J.E., "Stochastic Reduced Order Models with Python (SROMPy)" NASA/TM-2018-219824.

REPORT DOCUMENTATION PAGE

Form Approved
OMB No. 0704-0188

1. REPORT DATE *(DD-MM-YYYY)*
1-03-2020

2. REPORT TYPE
Technical Memorandum

3. DATES COVERED *(From - To)*

4. TITLE AND SUBTITLE

A 3D Model to Predict Explicit Morphologies and Volume Fraction of Lack-of-Fusion Pores Generated in Selective Laser Melting Processes

5a. CONTRACT NUMBER

5b. GRANT NUMBER

5c. PROGRAM ELEMENT NUMBER

6. AUTHOR(S)

Yeratapally, Saikumar R.; Cerrone, Albert, R.; Tang, Ming; Glaessgen, Edward H.;

5d. PROJECT NUMBER

5e. TASK NUMBER

5f. WORK UNIT NUMBER
109492.02.07.05.02

7. PERFORMING ORGANIZATION NAME(S) AND ADDRESS(ES)

NASA Langley Research Center
Hampton, VA 23681-2199

8. PERFORMING ORGANIZATION REPORT NUMBER
L-21131

9. SPONSORING/MONITORING AGENCY NAME(S) AND ADDRESS(ES)

National Aeronautics and Space Administration
Washington, DC 20546-0001

10. SPONSOR/MONITOR'S ACRONYM(S)
NASA

11. SPONSOR/MONITOR'S REPORT NUMBER(S)
NASA-TM-2020-220579

12. DISTRIBUTION/AVAILABILITY STATEMENT

Unclassified-
Subject Category 26
Availability: NASA STI Program (757) 864-9658

13. SUPPLEMENTARY NOTES

14. ABSTRACT

The performance of an additively manufactured (AM) component is dependent on the distribution of process-induced defects in addition to the complex microstructure of the material, surface roughness of the component and the process-induced residual stresses. For instance, it has been well demonstrated that lack-of-fusion (LoF) pores produced in the selective laser melting (SLM) AM process can significantly limit the fatigue performance of the material. Although two-dimensional (2D) models exist to predict the 2D profiles of LoF pores, the 2D pore profiles cannot be directly inserted into a three-dimensional (3D) microstructure domain that is output from several prevailing process simulation packages. A few commercial packages that simulate the SLM process can predict LoF pores in a 3D domain, but the morphologies of LoF pores are voxelated and hence do not capture sharp corners of the pores, thereby obviating their use in fatigue crack initiation studies. In order to address the aforementioned gaps, a high-fidelity model that predicts not only the volume fraction, but also the explicit 3D morphologies and spatial distributions of LoF pores has been developed using a computer aided design-based environment. The model has been partially validated for Ti-6Al-4V alloy by comparing the predictions of the volume fraction of LoF pores predicted by the model with experimental data obtained from the literature.

15. SUBJECT TERMS

Additive manufacturing; Lack-of-fusion; porosity prediction

16. SECURITY CLASSIFICATION OF:			17. LIMITATION OF ABSTRACT	18. NUMBER OF PAGES	19a. NAME OF RESPONSIBLE PERSON
a. REPORT	b. ABSTRACT	c. THIS PAGE			STI Help Desk (email: help@sti.nasa.gov)
U	U	U	UU	17	19b. TELEPHONE NUMBER *(Include area code)* (757) 864-9658